Acta Crystallographica Section A
Foundations of Crystallography
ISSN 0108-7673

Received 6 June 2012
Accepted 1 August 2012

Dynamical diffraction effect in a curved multi-plate crystal cavity

Y.-Y. Chang,[a] Y.-W. Tsai,[a] Y.-H. Wu,[a] M.-T. Tang[b] and S.-L. Chang[a,b]*

[a]Department of Physics, National Tsing Hua University, Taiwan, and [b]National Synchrotron Radiation Research Center, Hsinchu, Taiwan. Correspondence e-mail: slchang@phys.nthu.edu.tw

A modified algorithm for X-ray dynamical diffraction theory is presented for curved boundary crystals and a detailed description of the numerical procedure is given. The simulated and experimental results both show an anomalous focusing behavior in a curved multi-plate crystal cavity of silicon under the (12,4,0) back-diffraction condition at a photon energy of 14.4388 keV. The focusing effects are analyzed, within the framework of the dynamical theory of X-ray diffraction, from the excitation of the dispersion surface and modification of the index of refraction with respect to the non-plane-parallel boundaries of a curved crystal cavity.

1. Introduction

An X-ray Fabry–Perot-type resonator has recently been realised and the interference due to cavity resonance has been observed by using Si (12,4,0) back reflection for 14.4388 keV X-rays (Chang *et al.*, 2005). A curved multi-plate crystal cavity (Chang, Chen, Weng *et al.*, 2010; Chang, Chen, Wu *et al.*, 2010) was then developed by combining the X-ray Fabry–Perot crystal cavity with a compound refractive lens (CRL) (Snigirev *et al.*, 1996, 2009), aiming for focusing X-ray beams under resonance conditions. The former could confine X-rays inside the cavity to reach cavity resonance (Bond *et al.*, 1967; Kohn *et al.*, 2000; Chang *et al.*, 2006; Chen *et al.*, 2008). The latter, consisting of a linear array of lenses, is for common X-ray focusing *via* refraction. The curved multi-plate crystal cavity was designed by making the optical axis of the CRL perpendicular to the (12,4,0) back-reflection plane. As the X-ray beam passes through this crystal device under the back-diffraction condition, refraction and diffraction occur simultaneously, thus leading to resonance-enhanced beam focusing. To account for this enhanced beam focusing, we apply in this paper the dynamical diffraction theory to calculate the spatial and angular distributions of the transmitted beam through the crystal device. von Laue's treatment (von Laue, 1931) and the numerical algorithm of Stetsko & Chang (1997) are adopted. The Cartesian coordinate system is used to represent the X-ray wavefields and dispersion surface. The differences between curved multi-plate crystals and conventional plane-parallel crystal plates are taken into account by modifying the calculation algorithm. The major differences are: (i) the crystal surface is not parallel to the (12,4,0) atomic planes; (ii) the entrance and exit surfaces of the crystal device are not parallel to each other; and (iii) the slope of the crystal surface is varying. Since this kind of complicated crystal boundary has not been handled in dynamical calculations in detail in the literature, it is the purpose of this paper to propose a modified algorithm to solve the overall wavefields in a curved crystal and to apply it to a multi-plate crystal cavity. Experimental measurements of the transmitted beam through the curved crystal device are also shown and compared with the dynamical simulations.

2. Theory

In von Laue's dynamical theory, the atomic charges in a crystal were treated as continuous distributions and the dielectric susceptibility was represented as a periodic complex function. Furthermore, Maxwell's equations were used to deal with the interactions of X-rays with a crystal lattice by considering the dielectric susceptibility χ. The solutions of the wavefields to Maxwell's equations are assumed to be Bloch waves. Ultimately, one could obtain the fundamental equation of a wavefield for N diffracted beams (Stetsko & Chang, 1997; Authier, 2001; Chang, 2004):

$$(\mathbf{K}_m \cdot \mathbf{K}_m - k^2)\mathbf{E}_m = (\mathbf{K}_m \cdot \mathbf{E}_m)\mathbf{K}_m + k^2 \sum_n \chi_{m-n}\mathbf{E}_n, \qquad (1)$$

where $m = O, G_1, G_2, \ldots, G_{N-1}$, $\mathbf{K}_m$ are the wavevectors of the mth reflection inside the crystal and $\mathbf{E}_m$ is the corresponding electric field. For a given wavelength λ and a fixed incident angle, one can compute the excited wavefields inside the crystal by solving the fundamental equation. Then, by taking the entrance and exit boundary conditions into account, full information about the electromagnetic waves inside and outside the crystal can be obtained. For imperfect crystals, Takagi–Taupin equations need to be considered (Okitsu, 2003).

Based on the proposed algorithm (Stetsko & Chang, 1997), the vector form of the fundamental equation (1) can be decomposed into three scalar ones. Therefore, the fundamental equation can be solved as an eigenvalue equation of a

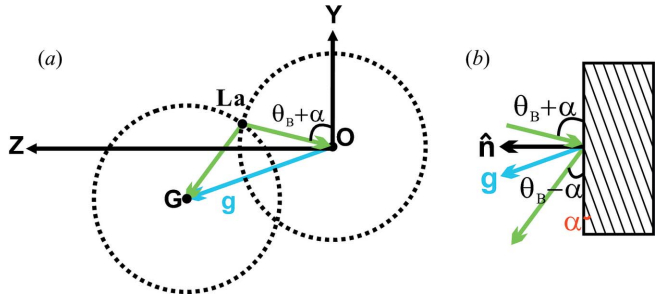

Figure 1
Geometric relationship of asymmetric two-beam diffraction in (*a*) reciprocal space and (*b*) real space.

matrix form with three scalars representing the x, y and z components of the Cartesian coordinates.

For a given set of atomic planes $G(hkl)$, the reciprocal-lattice vector is expressed as $\mathbf{g} = \mathbf{OG} = h\mathbf{a}^* + k\mathbf{b}^* + l\mathbf{c}^*$, where $O(000)$ is the origin of the reciprocal lattice. The reflection G can be symmetric or asymmetric, depending on whether the reciprocal-lattice vector $\mathbf{g}$ is parallel to the crystal surface normal $\mathbf{n}$. For an asymmetric reflection, the angle α between the atomic planes and the crystal surface is non-zero. In order to handle the boundary conditions more directly, the z axis is defined to be parallel to the direction $\mathbf{n}$ normal to the crystal surface and the x and y axes are arbitrarily chosen. Accordingly, the z components of the electric fields are perpendicular and the x and y components are parallel to the crystal surface. In this way the relative orientation of the reciprocal-lattice vector and the z axis of the Cartesian coordinates in the symmetric diffraction geometry is clearly different from that in the asymmetric case. Fig. 1 shows a two-beam diffraction geometry for a general situation with $\alpha \neq 0$. When $\mathbf{g}$ is parallel to $\mathbf{n}$, the z axis and $\mathbf{g}$ are parallel to each other. When $\mathbf{g}$ is not parallel to $\mathbf{n}$, the angle between the z axis and $\mathbf{g}$ is α.

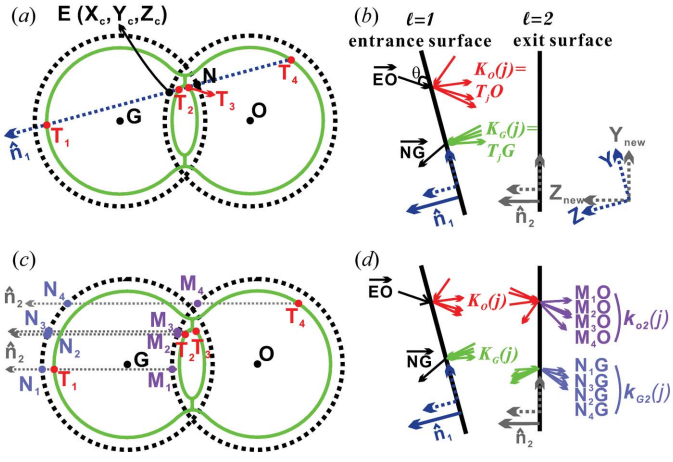

Figure 2
The excitation of the dispersion surface with respect to the entrance surface ($l = 1$) (*a*) and the exit surface ($l = 2$) (*c*), and the corresponding wavevectors, (*b*) and (*d*), inside and outside a crystal with non-parallel crystal boundaries for two-beam diffraction. In the case of back diffraction, the spheres centered at O and G are nearly tangential to each other at the center of the straight line **OG** and the Bragg angle is very close to $\pi/2$. This situation increases the width of the total reflection region.

After choosing the coordinates for the reciprocal space, the reciprocal-lattice points G_m of the mth reflection can be defined as (X_{Gm}, Y_{Gm}, Z_{Gm}). As shown in Fig. 1(*a*), the intersection of the two spheres of radius equal to $1/\lambda$ centered at the points $O(X_0, Y_0, Z_0)$ and $G(X_{G1}, Y_{G1}, Z_{G1})$ is the Laue point, denoted as La. The wavevectors **LaO** and **LaG** satisfy Bragg's condition, *i.e.* $\mathbf{LaG} = \mathbf{LaO} + \mathbf{g}$. The corresponding geometry in real space is shown in Fig. 1(*b*) where the incident angle is $\theta_B + \alpha$ and the outgoing angle is $\theta_B - \alpha$. θ_B is the Bragg angle of the G reflection.

For N-beam diffraction in the Bragg geometry, there are $4N$ excited tie points, namely $4N$ modes of wave propagation, thus leading to $4N$ diffracted waves and $4N$ transmitted waves inside the crystal. For simplicity, Fig. 2 is an example describing the relation between the dispersion surface and the wavevector in real and reciprocal space for two-beam diffraction with a σ-polarized incident wave. An incident beam $\mathbf{k}_0$ which impinges on the crystal at an incident angle (θ, ϕ) is represented as **EO** where E is the entrance point. The coordinates of point E are denoted as (X_c, Y_c, Z_c) in reciprocal space and defined as

$$(X_c, Y_c, Z_c) = \left(\frac{1}{\lambda}\cos\theta\sin\phi, \frac{1}{\lambda}\cos\theta\cos\phi, \frac{1}{\lambda}\sin\theta\right), \qquad (2)$$

where θ is the angle between the incident beam and the xy plane and ϕ is the angle between the y axis and the projection of the incident beam on the xy plane (Chiu *et al.*, 2008).

In reciprocal space, the incident beam **EO** excites the dispersion surface at tie points T_j along the entrance surface normal $\mathbf{n}_1$ and generates diffracted beams $\mathbf{T}_j\mathbf{G} = \mathbf{K}_G(j)$ and transmitted beams $\mathbf{T}_j\mathbf{O} = \mathbf{K}_O(j)$ inside the crystal, and the diffracted beam **NG** in front of the entrance surface.

As shown in Fig. 2(*a*), as $N = 2$ and the beam is σ-polarized, there are only four modes of wave propagation excited at the tie points labeled as T_1, T_2, T_3 and T_4, *i.e.*, T_j for $j = 1, \ldots, 4$. The coordinates of the tie point are (X_c, Y_c, z_j) where the X and Y coordinates are the same as that of the entrance point due to the continuity of the tangential components inside and outside the crystal at the boundary. In the case we deal with, ϕ is set to 0°, leading to $(X_c, Y_c, Z_c) = [0, (1/\lambda)\cos\theta, (1/\lambda)\sin\theta]$ and all the wavefields are located in the YZ plane.

When $\mathbf{K}_O(j)$ and $\mathbf{K}_G(j)$ arrive at the exit surface, they generate the outgoing wavevectors $\mathbf{k}_{o2}(j)$ and $\mathbf{k}_{G2}(j)$, respectively. The directions of these outgoing wavevectors are determined by the exit surface normal $\mathbf{n}_2$ due to the same reason as for the entrance surface. In other words, the exit points $M_1, \ldots, M_4$ on the sphere O and $N_1, \ldots, N_4$ on the sphere G are excited, as shown in Fig. 2(*c*), thus leading to the transmitted beams $\mathbf{M}_j\mathbf{O} = \mathbf{k}_{O2}(j)$ and the diffracted beams $\mathbf{N}_j\mathbf{G} = \mathbf{k}_{G2}(j)$ behind the exit surface. However, the z component of tie point T_j, z_j, is to be determined. The unknown z_j can be solved from the fundamental equation expressed in the following matrix form:

$$\begin{bmatrix} \mathbf{C}-z\mathbf{I} & \mathbf{0} & \mathbf{A}\mathbf{G}^{-2}\mathbf{A}-\mathbf{I} & \mathbf{A}\mathbf{G}^{-2}\mathbf{B} \\ \mathbf{0} & \mathbf{C}-z\mathbf{I} & \mathbf{B}\mathbf{G}^{-2}\mathbf{A} & \mathbf{B}\mathbf{G}^{-2}\mathbf{B}-\mathbf{I} \\ \mathbf{B}^2-\mathbf{G}^2 & -\mathbf{A}\mathbf{B} & \mathbf{C}-z\mathbf{I} & \mathbf{0} \\ -\mathbf{A}\mathbf{B} & \mathbf{A}^2-\mathbf{G}^2 & \mathbf{0} & \mathbf{C}-z\mathbf{I} \end{bmatrix} \begin{bmatrix} \mathbf{E}_x \\ \mathbf{E}_y \\ \mathbf{E}_v \\ \mathbf{E}_w \end{bmatrix} = (\mathbf{Q}_4 - z\mathbf{I})\mathbf{E}_4 = 0 \quad (3)$$

and

$$\mathbf{E}_z = -\mathbf{G}^{-2}(\mathbf{A}\mathbf{E}_v + \mathbf{B}\mathbf{E}_w), \quad (4)$$

where

$$\mathbf{E}_x = (E_O^x, E_{G_1}^x, \ldots, E_{G_{N-1}}^x)^T, \quad \mathbf{E}_y = (E_O^y, E_{G_1}^y, \ldots, E_{G_{N-1}}^y)^T,$$
$$\mathbf{E}_z = (E_O^z, E_{G_1}^z, \ldots, E_{G_{N-1}}^z)^T.$$

A, **B**, and **C** are diagonal matrices whose diagonal entries are $a_{mm} = x_m = X_{G_m} - X_c$, $b_{mm} = y_m = Y_{G_m} - Y_c$ and $c_{mm} = Z_{G_m}$, respectively. $\mathbf{G}^2 = \mathbf{k}^2(\mathbf{I} + \mathbf{F})$, where the entries of matrix **F** are $f_{mn} = \chi_{G_m - G_n}$.

Following the proposed algorithm (Stetsko & Chang, 1997), the fundamental equation is expressed as the scalar equation in a matrix form, equations (3) and (4), which can be solved as an eigenvalue problem. The eigenvalues z_j and eigenvectors ($\mathbf{E}_x$, $\mathbf{E}_y$, $\mathbf{E}_v$, $\mathbf{E}_w$) of the matrix $\mathbf{Q}_4$ represent the z values of the tie points and the excited electric fields inside the crystal. The real part of z_j determines the coordinates of tie points on the dispersion surface and the imaginary part corresponds to the absorption. The wavevector of the excited wave m for mode j is expressed as

$$\mathbf{K}_m(j) = \mathbf{T}_j\mathbf{m} = (X_m - X_c, Y_m - Y_c, Z_m - z_j) = (x_m, y_m, z_{mj}), \quad \text{where } m = O, G_1, G_2, \ldots, G_{N-1}. \quad (5)$$

Moreover, the z component of the electric field, $\mathbf{E}_z$, can be calculated from the eigenvector ($\mathbf{E}_v$, $\mathbf{E}_w$) given in equation (2). Thus, the electric fields associated with the wavevectors $\mathbf{K}_m(j)$ are expressed as $\mathbf{E}_m(j) = [E_m^x(j), E_m^y(j), E_m^z(j)]$. However, the eigenvectors give only the ratios among the electric fields $\mathbf{E}_m(j)$. The proportionality constants, C_j, are yet to be solved from the boundary conditions. Thus, the overall electric fields inside and outside the crystal can then be determined entirely. For solving C_j, one has to consider the entrance and exit boundaries together. However, when the two surfaces are not parallel to each other, the z axis of the entrance surface is not perpendicular to that of the exit surface. Under this circumstance the use of two different coordinate systems is essential in dealing with the two different boundaries.

At both boundaries, the continuities of the tangential components of the electric and magnetic fields, **E** and **H**, and of the normal components of the electric displacements **D** are employed. For the N-beam diffraction, the x, y and z components of the electric fields inside and outside the crystal are connected by the following boundary conditions:

$$\mathbf{D}_m = \varepsilon_0\left(\mathbf{E}_m + \sum_{n=0}^{N-1} \chi_{G_m - G_n}\mathbf{E}_n\right), \quad \mathbf{H}_m = \frac{1}{k}(\mathbf{K}_m \times \mathbf{E}_m). \quad (6)$$

At the entrance surface ($l = 1$) these relations are formulated as

$$\begin{aligned}
E^x&: \sum_{j=1}^{4N} c_j E_m^x(j) = E_{(i)}^x\delta_{mO} + E_{m1}^x \\
E^y&: \sum_{j=1}^{4N} c_j E_m^y(j) = E_{(i)}^y\delta_{mO} + E_{m1}^y \\
D^z&: \sum_{j=1}^{4N} c_j\left[E_m^z(j) + \sum_{n=0}^{N-1} \chi_{G_m - G_n}E_n^z(j)\right] = E_{(i)}^z\delta_{mO} + E_{m1}^z \\
H^x&: \sum_{j=1}^{4N} c_j[z_{mj}E_m^y(j) - y_m E_m^z(j)] \\
&\quad = (k_m^z E_{(i)}^y - y_m E_{(i)}^z)\delta_{mO} - (k_m^z E_{m1}^y + y_m E_{m1}^z) \\
H^y&: \sum_{j=1}^{4N} c_j[x_m E_m^z(j) - z_{mj}E_m^x(j)] \\
&\quad = (x_m E_{(i)}^z - k_m^z E_{(i)}^x)\delta_{mO} + (x_m E_{m1}^z + k_m^z E_{m1}^x), \quad (7)
\end{aligned}$$

where $(E_{(i)}^x, E_{(i)}^y, E_{(i)}^z)$ is the electric field of the incident wave and $(E_{m1}^x, E_{m1}^y, E_{m1}^z)$ are the electric fields of the diffracted waves m in front of the entrance surface ($l = 1$) with the wavevector $\mathbf{k}_m = (x_m, y_m, -k_m^z)$, where $k_m^z = -[k^2 - (x_m^2 + y_m^2)]^{1/2}$. Since $\mathbf{r}_1$ is a null vector, the wavefunctions $\psi_{m1}(j) = \exp(-2\pi i\mathbf{K}_m \cdot \mathbf{r}_1)$ and $\varphi_{m1} = \exp(-2\pi i\mathbf{k}_m \cdot \mathbf{r}_1)$ are equal to 1 and are omitted in equation (7).

On the other hand, at the exit surface all the components of the wavefields are defined by a new coordinate system where the new z axis is perpendicular to the exit surface shown in Fig. 2(*b*). The new coordinate system is constructed by using the rotation matrix as follows:

$$\begin{bmatrix} x'_m \\ y'_m \\ z'_{mj} \end{bmatrix} = \begin{bmatrix} 1 & 0 & 0 \\ 0 & \cos\omega & \sin\omega \\ 0 & -\sin\omega & \cos\omega \end{bmatrix} \begin{bmatrix} x_m \\ y_m \\ z_{mj} \end{bmatrix} = \begin{bmatrix} x_m \\ y_m\cos\omega + z_{mj}\sin\omega \\ -y_m\sin\omega + z_{mj}\cos\omega \end{bmatrix}. \quad (8)$$

The new coordinates are then labeled with primes. Since the two boundaries are not parallel to each other, the wavevectors of the transmitted and diffracted beams are split into $4N$ directions after going through the exit surface. Fig. 2(*d*) shows four splitting beams separately in a two-beam (O, G) diffraction with a σ-polarized incident wave. In other words, the beam splitting leads to the situation in which each excited mode should be calculated separately while dealing with the exit boundary conditions. In addition, the new x'_m and y'_m are possibly complex numbers due to the coordinate transformation, namely, the z component of the wavevector outside the exit surface is defined as

$$k_m'^z = -\left(k^2 - [Re(x'_m)^2 + Re(y'_m)^2]\right)^{1/2}. \quad (9)$$

At the exit surface ($l = 2$) the boundary conditions are formulated as

$$
\begin{aligned}
&E'^{x}\colon\ c_j E'^{x}_{m}(j)\psi_{m2}(j) = E'^{x}_{m2}(j)\varphi_{m2}(j)\\
&E'^{y}\colon\ c_j E'^{y}_{m}(j)\psi_{m2}(j) = E'^{y}_{m2}(j)\varphi_{m2}(j)\\
&D'^{z}\colon\ c_j\left[E'^{z}_{m}(j) + \sum_{n=0}^{N-1}\chi_{G_m-G_n}E'^{z}_{n}(j)\right]\psi_{m2}(j) = E'^{z}_{m2}(j)\varphi_{m2}(j)\\
&H'^{x}\colon\ c_j[z'_{mj}E'^{y}_{m}(j) - y'_{mj}E'^{z}_{m}(j)]\psi_{m2}(j)\\
&\qquad = [Re(k'^{z}_{mj})E'^{y}_{m2}(j) - Re(y'_{mj})E'^{z}_{m2}(j)]\varphi_{m2}(j)\\
&H'^{y}\colon\ c_j[x'_{mj}E'^{z}_{m}(j) - z'_{mj}E'^{x}_{m}(j)]\psi_{m2}(j)\\
&\qquad = [Re(x'_{mj})E'^{z}_{m2}(j) - Re(k'^{z}_{mj})E'^{x}_{m2}(j)]\varphi_{m2}(j), \qquad (10)
\end{aligned}
$$

where $j = 1, \ldots, 4N$, $\psi_{m2}(j) = \exp[-2\pi i\mathbf{K}'_m(j)\cdot\mathbf{r}'_2]$, $\varphi_{m2}(j) = \exp[-2\pi i\mathbf{k}'_m(j)\cdot\mathbf{r}'_2]$, $\mathbf{K}'_m(j) = (x'_{mj}, y'_{mj}, z'_{mj})$ and $\mathbf{k}'_m(j) = [Re(x'_{mj}), Re(y'_{mj}), k'^{z}_{m}]$. In the new coordinate system, $\mathbf{K}'_m$ and $\mathbf{k}'_m$ are, respectively, the wavevectors inside and outside the crystal and $\mathbf{r}'_2$ is the position vector of the exit point. The total number of unknowns in equations (7) and (10) is $10N$, including $4N$ unknown C_j and $6N$ unknown components of the electric fields, $(E^{x}_{ml}, E^{y}_{ml}, E^{z}_{ml})$ and $(E'^{x}_{m2}, E'^{y}_{m2}, E'^{z}_{m2})$, in front of the entrance surface and behind the exit surface, respectively.

The next step is to solve the unknown C_j. By combining the first and third equations into the fifth one in equation (7), the unknowns E^{x}_{m1} and E^{z}_{m1} are eliminated. The same procedure was implemented for the rest of equations (7) and (10). Finally, the simplified equations are

$$
\begin{aligned}
&\sum_{j=1}^{4N} c_j\left\{[z_{mj} + k^{z}_{m}]E^{x}_{m}(j) + x_m\sum_{n=0}^{N-1}\chi_{G_m-G_n}E^{z}_{n}(j)\right\} = 2k^{z}_{m}E^{x}_{(i)}\delta_{mO}\\
&\sum_{j=1}^{4N} c_j\left\{[z_{mj} + k^{z}_{m}]E^{y}_{m}(j) + y_m\sum_{n=0}^{N-1}\chi_{G_m-G_n}E^{z}_{n}(j)\right\} = 2k^{z}_{m}E^{y}_{(i)}\delta_{mO}\\
&\sum_{j=1}^{4N} c_j\left\{[z'_{mj} - k'^{z}_{m}(j)]E'^{x}_{m}(j) + Re[x'_{m}(j)]\sum_{n=0}^{N-1}\chi_{G_m-G_n}E'^{z}_{n}(j)\right.\\
&\qquad \left. + Im[x'_{m}(j)]E'^{z}_{m}(j)\right\}\exp[-i2\pi\mathbf{K}'_{m2}(j)\cdot\mathbf{r}'_2] = 0\\
&\sum_{j=1}^{4N} c_j\left\{[z'_{mj} - k'^{z}_{m}(j)]E'^{y}_{m}(j) + Re[y'_{m}(j)]\sum_{n=0}^{N-1}\chi_{G_m-G_n}E'^{z}_{n}(j)\right.\\
&\qquad \left. - Im[y'_{m}(j)]E'^{z}_{m}(j)\right\}\exp[-i2\pi\mathbf{K}'_{m2}(j)\cdot\mathbf{r}'_2] = 0. \qquad (11)
\end{aligned}
$$

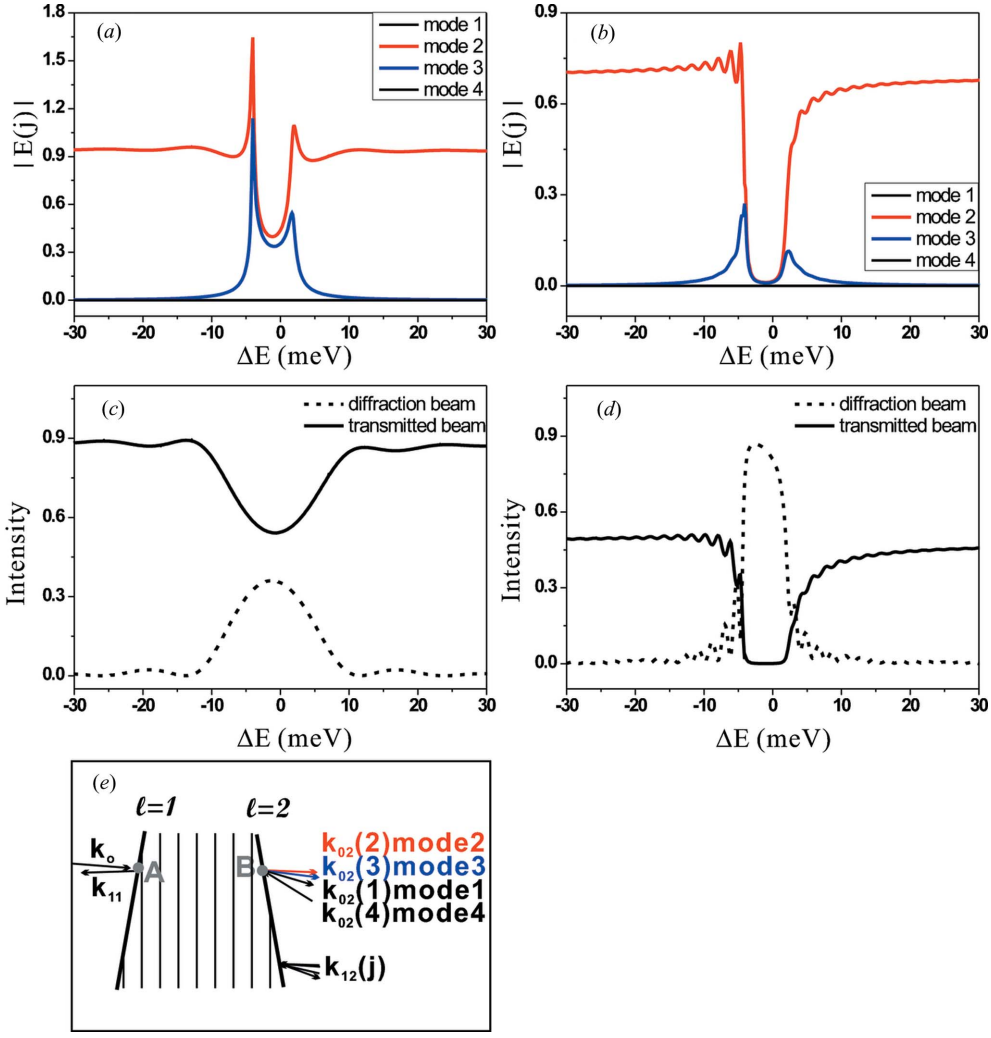

Figure 3
Simulations of the electric field and intensity of Si (12,4,0) back diffraction in trapezoid crystals: (*a*) and (*c*) for 50 µm, and (*b*) and (*d*) for 300 µm crystal thickness. (*e*) Schematic of the wavevectors in front of and behind a trapezoid crystal.

There are $4N$ equations which exactly correspond to $4N$ unknown C_j. After solving the C_j, one can substitute C_j into equations (7) and (10) to obtain all the components of the electric fields outside the crystal.

3. Simulation

3.1. Trapezoid crystal

Fig. 3 shows the simulation for (12,4,0) back diffraction with a σ-polarized incident wave in trapezoid crystals of thicknesses 50 and 300 µm for a photon energy around 14.4388 keV. Figs. 3(*a*) and (*b*) display the absolute value of the transmitted electric field of each individual mode as a function of the X-ray energy. The simulation results show that the excitations of modes 1 and 4 are almost zero, so the dominant modes are modes 2 and 3 for the transmitted beam. However, by comparing the transmitted electric field of mode 3 for the two different thicknesses, one can find that an increase in thickness makes mode 3 weaker. The reason comes from the direction of the Poynting vector, which describes the energy flow of the wavefield. The Poynting vector is labeled as $\mathbf{S}_j$ for the jth mode. The energy flow directs towards the interior of the crystal by $\mathbf{S}_2$ and points out of the crystal by $\mathbf{S}_3$. However, when the crystal thickness is too thick, the absorption effect makes $\mathbf{S}_3$ almost disappear. Therefore, mode 3 exists with an appreciable amplitude only in a thin crystal. Figs. 3(*c*) and (*d*) show the transmitted and back-diffracted intensities as a function of X-ray energy at the outgoing point B and incident point A (see Fig. 3*e*). It shows that the (12,4,0) back diffraction occurs within an energy range of about $\Delta E = \pm 15$ meV. In this range, the non-parallel boundaries cause the transmitted beam splitting, while the diffraction beam is kept along the same direction as shown schematically in Fig. 3(*e*).

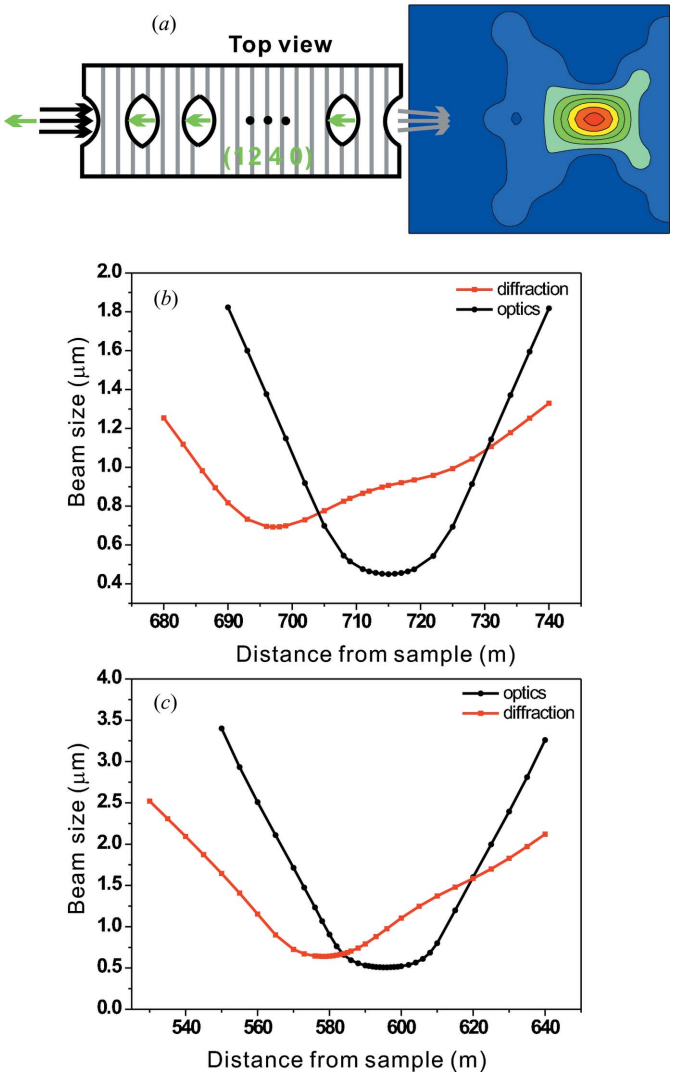

Figure 4
(*a*) The top view of the refractive lens of Si (left) and the intensity distribution of the transmitted beam at the exit end of the lens. Calculated beam sizes at $\Delta E = 5$ meV at the exit end of the lens with (red line) and without (black line) the (12,4,0) back diffraction in two different designs: (*b*) device 1 and (*c*) device 2 (the accuracy of the beam-size calculation is 0.1 µm).

Table 1
The different designs of compound refractive lenses.

t and g are the thickness and gap of the parabola apex, respectively, R is the radius of the parabola apex, and N is the number of lenses.

Device No.	t (µm)	g (µm)	R (µm)	N	$f_{\rm optics}$ (mm)
1	10	90	40	12	715
2	20	180	25	9	596

3.2. Curved crystal

Crystal devices consisting of compound refractive lenses as shown in Fig. 4(*a*) are designed to observe the influence of beam focusing due to the curved boundaries for X-ray back diffraction. The atomic plane (12,4,0) of Si is chosen as the back reflection at the photon energy of 14.4388 keV. The optical axis of the lens is designed to be along [12,4,0]. Therefore, beam focusing is accompanied with back diffraction when the transmitted beam passes through the crystal devices. There are two different parameters listed in Table 1 for the focusing crystal devices. The formula $f_{\rm optics} = R/2N\delta$ is used to estimate the ideal focal length of optical refraction, where δ is the correction of the real part of refractive index ($n = 1 - \delta + i\beta$) (Als-Nielsen & McMorrow, 2001; Schroer *et al.*, 2005).

The simulation for beam focusing is carried out by using the above-mentioned dynamical theory for asymmetric and nonparallel boundaries. On the curved surface, an incident beam with a horizontal beam size of 120 µm is divided into several wavelets, each of which has a beam size of 0.1 µm. After solving the electric field and wavevector inside and outside the crystal, all of the outgoing waves are integrated to give a two-dimensional intensity mapping of the transmitted beam through the focusing device. Fig. 4(*a*) simply depicts the layout of the crystal device and the intensity mapping. From the intensity distribution, the variation of the horizontal beam size along the [000] direction can be extracted. Figs. 4(*b*) and

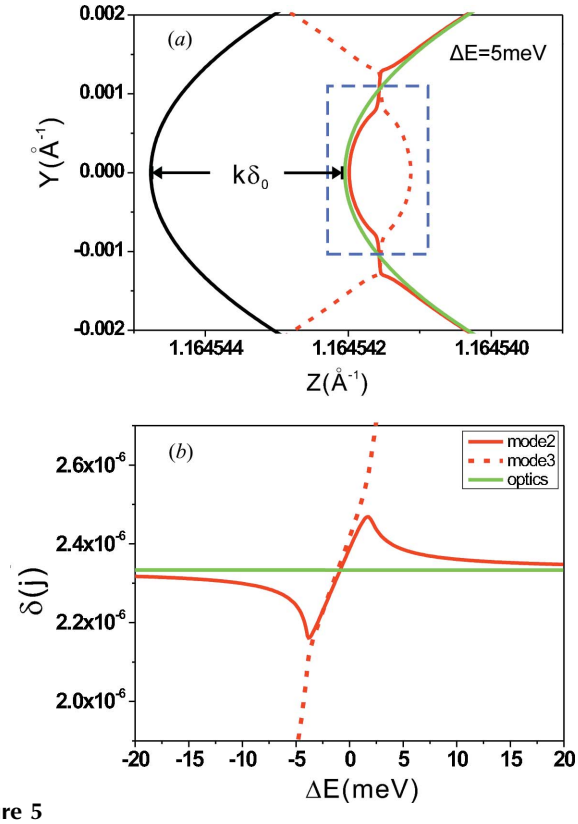

Figure 5
(*a*) The dispersion surface at $\Delta E = 5$ meV deviation from 14438.8 eV: the red line is for (12,4,0) back diffraction and the green one is for the one-beam case (without diffraction). (*b*) The calculation of $\delta(j)$ as a function of the energy deviation from 14438.8 eV.

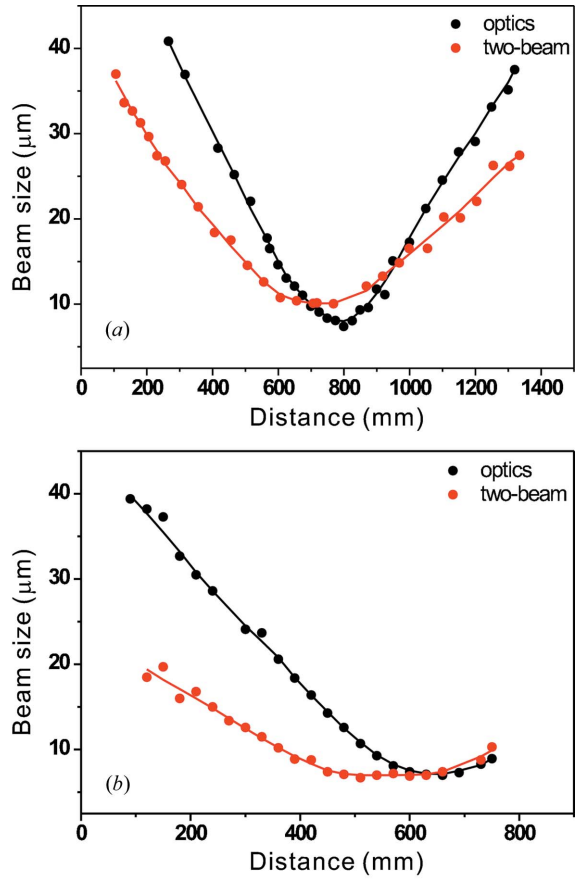

Figure 6
The beam-size measurements of the two designed crystal devices: (*a*) device 1 and (*b*) device 2 ($\Delta E \simeq 5$ meV).

4(*c*) show the calculated beam sizes of the two different crystal devices, respectively, where the red and black dotted lines indicate the beam sizes with and without back diffraction (optical refraction). We assume that the integrated intensity of the incident beam is 1. Then the integrated intensities of the transmitted beams through devices 1 and 2 at the focal point are 0.086 and 0.12 for the diffraction case and 0.163 and 0.377 for the optics case. As is clearly seen, the two devices exhibit the similar behavior of having a reduced focal length under the back-diffraction condition.

This anomalous focusing phenomenon can be understood by analyzing the excitation of the dispersion surface. The coordinates of a point on the dispersion surface are determined from the difference between the wavevectors inside and outside the crystal. In other words, it gives information about the variation of the refractive index as a function of z. In Fig. 5(*a*), the black and green curves show some portions of the Ewald spheres outside and inside the crystal. The difference between them is $k - n_0 k$ ($= k\delta_0$). When the geometry satisfies the diffraction condition, the dispersion surface (red curve) is excited rather than the green curve. Therefore, the refractive behavior under the diffraction condition is not like the conventional optical refraction, because there are several modes with $\delta(j)$ [or $n(j)$] different from δ_0 (n_0).

Fig. 5(*b*) depicts the calculated $\delta(j)$ as a function of the energy in the vicinity of the exact energy, $E_{\rm exact}$(= 14438.8 eV), of the (12,4,0) back reflection. $\delta(2)$ and $\delta(3)$ are derived from the excitations of mode 2 and 3, respectively. Compared to δ_0, the value of $\delta(j)$ varies drastically around $E_{\rm exact}$. At energies far away from $E_{\rm exact}$, $\delta(2)$ approaches δ_0 and $\delta(3)$ disperses. When E is higher than $E_{\rm exact}$, $\delta(2)$ and $\delta(3)$ are larger than δ_0. Under this condition, the beam focusing can be enhanced and the focal length is reduced. From the analysis of $\delta(j)$, the focusing enhancement at the back-diffraction condition can be qualitatively explained.

4. Experiment

To observe the focusing behavior in a compound refractive lens using back diffraction of (12,4,0) at 14.4388 keV, an experiment was carried out at the Taiwan undulator beamline BL12XU at SPring-8. The synchrotron radiation was first monochromated by a double-crystal monochromator and then by an ultra-high-resolution monochromator to give an energy resolution $\Delta E/E \simeq 2.5 \times 10^{-8}$ at 14.4388 keV (Yabashi *et al.*, 2001; Ishikawaa *et al.*, 2005; Chang *et al.*, 2006). The crystal devices were manufactured from an Si (001) wafer using microelectronic lithography and dry etching processes. The detailed experiment has been reported in Chang, Chen, Weng *et al.* (2010) and Chang, Chen, Wu *et al.* (2010). The horizontal beam sizes of the transmitted beam at various distances behind the focusing lens were measured by a knife edge to

determine the focal point. In Fig. 6(*a*), the red dots and black dots show the beam-size measurements with and without, respectively, the back diffraction for crystal device 1. As a result, the focal length for two-beam back diffraction is reduced by about 10–13% compared to that for optical refraction. The observation is in agreement with the theoretical simulation. Similar results are obtained for the beam sizes measured for crystal device 2 in Fig. 6(*b*).

5. Conclusion

We have presented in this paper a modified algorithm for dynamical diffraction for the complicated boundary conditions encountered for a curved crystal surface. The calculations based on this algorithm show that the dynamical diffraction effect causing the beam splitting in the transmitted direction is due to the non-parallel crystal boundaries and the variation of the refractive indices $n(j)$ from the normal value n_0 during the excitation of N modes of wave propagation. By the same token, the enhanced focusing effect in a curved multi-plate crystal cavity consisting of compound refractive lenses can also be explained. Furthermore, since the variation of refractive indices is very sensitive to X-ray energy, one could apply the dynamical diffraction effect to design other optical devices, such as a high-resolution X-ray prism.

We thank M. Yabashi, N. Hiraoka and C.-C. Chen for technical support, and the Ministry of Education and National Science Council (NSC) of Taiwan, ROC, for financial support.

References

Als-Nielsen, J. & McMorrow, D. (2001). *Elements of Modern X-ray Physics.* New York: Wiley.

Authier, A. (2001). *Dynamical Theory of X-ray Diffraction.* Oxford, New York: Oxford University Press.

Bond, W. L., Duguay, M. A. & Rentzepis, P. M. (1967). *Appl. Phys. Lett.* **10**, 216–218.

Chang, S.-L. (2004). *X-ray Multiple-Wave Diffraction: Theory and Application*, ch. 7. Berlin: Springer-Verlag.

Chang, S.-L., Stesko, Yu. P., Tang, M.-T., Lee, Y.-R., Sun, W.-H., Yabashi, M. & Ishikawa, T. (2005). *Phys. Rev. Lett.* **94**, 174801.

Chang, S.-L., Stesko, Yu. P., Tang, M.-T., Lee, Y.-R., Sun, W.-H., Yabashi, M., Ishikawa, T., Wu, H.-H., Shew, B.-Y., Lin, Y.-H., Kuo, T.-T., Tamssaku, K., Miwa, D., Chen, S.-Y., Chang, Y.-Y. & Shy, J.-T. (2006). *Phys. Rev. B*, **74**, 134111.

Chang, Y.-Y., Chen, S.-Y., Weng, S.-C., Chu, C.-H., Tang, M.-T., Stetsko, Yu. P, Shew, B.-Y., Yabashi, M. & Chang, S.-L. (2010). *X-ray Opt. Instrum.* **2010**, doi: 10.1155/2010/421945.

Chang, Y.-Y., Chen, S.-Y., Wu, H.-H., Weng, S.-C., Chu, C.-H., Lee, Y.-R., Tang, M.-T., Stetsko, Yu. P., Shew, B.-Y., Yabashi, M. & Chang, S.-L. (2010). *Opt. Express*, **18**, 7886–7892.

Chen, S.-Y., Wu, H.-H., Chang, Y.-Y., Lee, Y.-R., Sun, W.-H., Chang, S.-L., Stetsko, Yu. P., Tang, M.-T., Yabashi, M. & Ishikawa, T. (2008). *Appl. Phys. Lett.* **93**, 141105.

Chiu, M.-S., Stetsko, Yu. P. & Chang, S.-L. (2008). *Acta Cryst.* A**64**, 394–403.

Ishikawaa, T., Tamasakua, K. & Yabashi, M. (2005). *Nucl. Instrum. Methods A*, **547**, 42–49.

Kohn, V. G., Shvydko, Yu. V. & Gerdau, E. (2000). *Phys. Status Solidi B*, **221**, 597–615.

Laue, M. von (1931). *Ergeb. Exakten Naturwiss.* **10**, 133–158.

Okitsu, K. (2003). *Acta Cryst.* A**59**, 235–244.

Schroer, C. G., Kurapova, O., Patommel, J., Boye, P., Feldkamp, J., Lengeler, B., Burghammer, M., Riekel, C., Vincze, L., Van der Hart, A. & Kuchler, M. (2005). *Appl. Phys. Lett.* **87**, 124103.

Snigirev, A., Kohn, V., Snigireva, I. & Lengeler, B. (1996). *Nature (London)*, **384**, 49–51.

Snigirev, A., Snigireva, I., Kohn, V., Yunkin, V., Kuznetsov, S., Grigoriev, M. B., Roth, T., Vaughan, G. & Detlefs, C. (2009). *Phys. Rev. Lett.* **103**, 064801.

Stetsko, Yu. P. & Chang, S.-L. (1997). *Acta Cryst.* A**53**, 28–34.

Yabashi, M., Tamasaku, K., Kikuta, S. & Ishikawa, T. (2001). *Rev. Sci. Instrum.* **72**, 4080–4083.